Journal of Materials Chemistry B

Accepted Manuscript

ROYAL SOCIETY OF CHEMISTRY

www.rsc.org/materialsB

Fe_3O_4@mSiO_2 Core-Shell Nanocomposite Capped with Disulfide Gatekeepers for Enzyme-Sensitive Controlled Release of Anti-Cancer Drug

Chunyu Yang[†], Wei Guo[†], Liru Cui[§], Na An[§], Ting Zhang[§],

Gang Guo[§]*, Huiming Lin[†]* and Fengyu Qu[†]*

[†] Department of Photoelectric Band Gap Materials Key Laboratory of Ministry of Education, Harbin Normal University, Harbin 150025, China

[§] College of Chemistry and Chemical Engineering, Harbin Normal University, Harbin 150025, China

***To whom all correspondence should be addressed.** Tel: (+86) 451-88060653. E-mail: qufengyu@hrbnu.edu.cn, linhuiming@hrbnu.edu.cn , and guogang19761126@sina.com

Abstract

Multifunctional nanocarriers based on the magnetic Fe_3O_4 nanoparticle core and bis-(3-carboxy-4-hydroxy phenyl) disulfide (R-S-S-R_1) modified mesoporous silica shell (Fe_3O_4@$mSiO_2$@R-S-S-R_1) were synthesized for cancer treatment, including passive targeting and enzyme-sensitive drug release. Anti-cancer drug doxorubicin (DOX) was used as the model cargo to reveal the release behavior of the system. The drug loading system (DOX-Fe_3O_4@$mSiO_2$@R-S-S-R_1) retains the drug until it reaches the tumor tissue where glutathione reductase (GSH) can degrade disulfide bond and make drug release. Furthermore, the grafting-amount of R-S-S-R_1 can be used to adjust the release performance. All the release behaviors fit the Higuchi model very well and the release kinetics is predominated by disulfide bond degradation and mesoporous structure. With good bioactivity and targeted release performance, the system could play an important role in the development intracellular delivery nanodevices for cancer therapy.

Introduction

The development of diverse kinds of nanoscale drug delivery systems such as polymers,[1] micelles,[2] liposomes,[3] dendrimers[4] and inorganic materials[5] for cancer treatment has been received expanding attention and has become a major field in medical research in recent years. Among these, the burgeoning interests in mesoporous silica nanoparticles (MSNs) has been greatly spurred due to their flexible and robust properties, including easily modification, excellent chemical stability, and outstanding biocompatibility.[6-10] Moreover, the uniform and tunable morphology/pore size, high pore volume, large surface area for MSNs ensure high loading of various drug molecules as well as smart transporting.[11-14] However, pure MSNs materials always face some practical applicability limitation due to the premature or burst drug release within several hours after incubation *in vitro*.[15] Therefore, the intriguing concept of stimulus-responsive gatekeeping was introduced to regulate the cargo release and to optimize the application of MSNs on nanomedicine. Presently, nanoparticles, organic molecules and supramolecular nanovalves have been employed as "gatekeepers" for MSNs to show the well-controlled release performance, and the controlled-release process can be regulated either by external stimuli such as thermal, light, electrostatic, magnetic actuation, photoirradiation, or by internal stimuli such as pH and enzymes etc.[16-20] For instance, Yang and his co-workers have constructed a novel cancer theranostic hybrid platform, based on mesoporous silica-coated gold nanorods gated by sulfonatocalix [4] arene switches, for biofriendly near-infrared (NIR) light-triggered cargo release in a remote and stepwise fashion.[21] And zhu et al.

successfully demonstrated a pH-triggered controlled drug release system by the dissolution of ZnO nanolids in acidic condition, showing a valuable pH-responsive strategy for the delivery of anticancer agents.[22]

The disulfide bond was systemically nontoxic and stable in blood circulation, and it can only be degraded by reduced glutathione or others thiols compounds with certain concentration.[23,24] Furthermore, the concentration of GSH is often elevated to 2-10 mM[25,26] about 2 times in tumor tissues[27,28] than that in normal tissues, so that the disulfide is attractive to be used in the targeted release on tumor tissues. For example, Yang et al. have described the preparation of a core/shell multi-sensitive composite nanoparticles with poly(N-vinylcaprolactam-s-s-methacrylic acid) (P-(VCL-s-s-MAA)) shell to reveal the sensitive release behavior for cancer treatment.[15]

Magnetic (Fe_3O_4 or γ-Fe_2O_3) nanoparticles with strong magnetic property and low toxicity have been most intensively studied as targeted and magnetic resonance imaging agents.[29-32] However, pure iron oxide is prone to aggregation due to anisotropic dipolar attraction and rapid biodegradation when they are exposed to biological systems directly.[33,34] The core-shell structure with iron oxide nanoparticle as core and mesoporous silica as shell not only can overcome the limitation of pure iron oxide nanoparticles but also can combine the advantages of the two to improve the performance in the field of targeted drug delivery.[35,36] Due to the collateral damages and adverse side effects of most cancer drugs, the targeting drug delivery system have attracted many attentions on cancer therapy.[37] For example, Yang et al.

have designed a novel fibrous-structured mesoporous silica microspheres (denoted as Fe_3O_4/FMSMs), which exhibit a sustained drug release profile, sufficient magnetic responsivity and redispersibility to the external magnetic field. And Wang and coworkers have synthesized a bicontrollable drug release system with PAH/PSS multilayers on to $Fe_3O_4/mSiO_2$, showing the magnetic-targeted and pH-controllable release behavior.

With all of these considerations in mind, we synthesized a $Fe_3O_4@mSiO_2$ nanocarrier consisted of magnetic Fe_3O_4 nanoparticle core and mesoporous silica ($mSiO_2$) shell, showing passive targeting property (Fe_3O_4 target) associated with enzyme-sensitive controlled release. As shown in Scheme 1, in the first step, the core-shell $Fe_3O_4@mSiO_2$ nanomaterials were prepared as the drug carriers. At the same time, the synthesized bis-(3-carboxy-4-hydroxy phenyl) disulfide was modified with an amino silane coupling agent (3-aminopropyltriethoxysilane) which was denoted as (R-S-S-R_1). After the drug (DOX) loading, the enzyme-sensitive R-S-S-R_1 was employed to graft outside of the $Fe_3O_4@mSiO_2$ as the blocking agent to inhibit premature drug release. It is known that, the high expression of glutathione reductase (GSH)[38] in tumor tissue promotes the degradation of -S-S-, thereby allowing the release of DOX.

Experiment and methods

Materials

Unless specified, all of the chemicals used were analytical grade and used without further purification. Cetyltrimethylammonium bromide (CTAB), tetraethyl

orthosilicate (TEOS), 3-[4,5-dimethylthialzol-2-yl]-2,5-diphenyltetrazolium bromide (MTT), doxorubicin hydrochloride (DOX), 2'-(4-ethoxyphenyl)-5-(4-methyl-1-piperazinyl)-2,5'-bi-1H-benzimidazole, trihydrochloride (Hoechst 33342), N,N'-dicyclohexylcarbodiimide (DCC), 4-dimethylaminopyridine (DMAP), (3-aminopropyl)triethoxysilane (APTES), sodium oleate, oleic acid, 1-octadecene, 5-aminosalicyclic acid, sodium nitrite, potasium xantogenate, dichloromethane, ethyl acetate, petroleum ether were obtained from Aladdin, China. Ferric trichloride hexahydrate ($FeCl_3 \cdot 6H_2O$), ethanol, n-hexane and triethylamine were purchased from Tianjin Chemical Corp. of China.

Synthesis of iron-oleate complex

In a typical synthesis of iron-oleate complex, 10.8 g of iron chloride ($FeCl_3 \cdot 6H_2O$, 40 mmol) and 36.5 g of sodium oleate (120 mmol, 95 %) was dissolved in a mixture solvent composed of 80 mL ethanol, 60 mL distilled water and 140 mL hexane. The resulting solution was heated to 70 ℃ and kept at that temperature for 4 h. When the reaction was completed, the upper organic layer containing the iron-oleate complex was washed three times with 30 mL distilled water in a separatory funnel. After washing, hexane was evaporated off, resulting in iron-oleate complex in a waxy solid form.

Synthesis of Fe_3O_4 nanoparticles

Following a literature procedure, Fe_3O_4 nanoparticles were prepared.[39] 36 g (40 mmol) of the iron-oleate and 5.7 g of oleic acid (20 mmol, 90 %) were dissolved in 200 g of 1-octadecene (90 %) at room temperature. The reaction mixture was heated to 320 ℃

with a constant heating rate of 3.3 °C min^{-1}, and then kept at that temperature for 30 min. When the reaction temperature reached 320 °C, a severe reaction occurred and the initial transparent solution became turbid and brownish black. The resulting solution containing the nanocrystals was then cooled to room temperature, and 500 mL of ethanol was added to the solution to precipitate the nanocrystals, which were further collected by centrifugation and then dispersed in chloroform.

Synthesis of Fe_3O_4@mSiO_2 nanoparticles

In a typical procedure, 0.5 mL of the Fe_3O_4 nanocrystals in chloroform (10 mg mL^{-1}) was poured into 8 mL of 0.2 M aqueous CTAB solution and the resulting solution was stirred vigorously for 30 min. The formation of an oil-in-water microemulsion resulted in a turbid brown solution. Then, the mixture was heated up to 60 °C for 30 min to evaporate the chloroform, resulting in a transparent black Fe_3O_4/CTAB solution. Then, 20 mL distilled water was added to the obtained black solution and the pH value of the mixture was adjusted to 8-9 by using 0.1 M NaOH. After that, 100 µL of 20 % TEOS in ethanol was injected six times at a 30 min intervals. The reaction mixture was reacted for 24 h under violent stirring. The obtained Fe_3O_4@mSiO_2 NPs were centrifuged and rinsed with ethanol repeatedly to remove the excess precursors and CTAB molecules and then dispersed in ethanol (8 mL).

Synthesis of bis-(3-carboxy-4-hydroxy phenyl) disulfide (named as R-S-S-R)

Disulfide was prepared starting from 5-ASA through the preparation of the xantogenate derivative (see Fig. S1).[40,41] In a three necked round bottomed flask, 5-aminosalicyclic acid (5.0 g, 0.03 mol, 1eq) was suspended in water (17 mL) and

acidified with concentrated hydrochloric acid (13 mL). The mixture was cooled to 0 °C. A solution of sodium nitrite (2.3 g, 0.03 mol, 1eq) in water (16 mL) was added dropwise to the acididic solution, keeping the temperature below 5 °C. The mixture was stirred for 1.5 h. The reaction pH was then raised to 5 using sodium hydroxide sodium (50 %) under the temperature below 5 °C. Potasium xantogenate (15.70 g, 3eq) was dissolved in water (15 mL) under nitrogen at room temperature; the cooled diazonium solution was added dropwise to the solution. The solution turned red and nitrogen gas was released. The reaction mixture was stirred for an additional hour at room temperature. Dichloromethane was added and the mixture was acidified using 1 M hydrochloric acid. The organic phase was separated, extracted with brine, separated, dried and evaporated under reduced pressure. The residue was purified by flash column chromatography (PE: EA= 5:1) to give the xantogenate product (5.24 g, 62.16 %). Product was dissolved in ethanol (22 mL) to give a red colored solution. Potassium hydroxide (3.41 g, 3eq) was added into this solution. The solution was stirred for 5 h then acidified with 1 M HCl and extracted with ethyl acetate. The organic layer was separated, dried and evaporated. The crude product was purified by flash column chromatography on silica gel (PE: EA= 1:1) to obtain disulfide (1.42 g, 12.85 %). The NMR spectrum of as-synthesized R-S-S-R is shown in Fig. S2.

Synthesis of R-S-S-R-APTES (named as R-S-S-R_1)

In a typical procedure, 3.718 g (0.011 mol) of R-S-S-R were dissolved in 50 mL of dimethyl sulfoxide at room temperature. When it is completely dissolved, 2.269 g (0.011 mol) of N,N'-dicyclohexylcarbodiimide (DCC) was added and then kept at that

temperature for 1 h. Then, 4.807 g (0.022 mol) of (3-aminopropyl)triethoxysilane (APTES) and 0.1222 g (0.001 mol) of 4-dimethylaminopyridine (DMAP) were added dropwise to the solution, the reaction mixture was reacted for 28 h under stirring.

Drug loading and synthesis of DOX-Fe_3O_4@mSiO_2@R-S-S-R_1

Fe_3O_4@mSiO_2 (60 mg) and DOX (3 mg) were added to the ethanol solution (3 mL) and stirred at 25 °C for 12 h. And then, 150, 250 and 500 μL supernatant fluid of R-S-S-R_1 was added to the mixed solution. The obtained solid (named as DOX-Fe_3O_4@mSiO_2@R-S-S-R_1-1, DOX-Fe_3O_4@mSiO_2@R-S-S-R_1-2, DOX-Fe_3O_4@mSiO_2@R-S-S-R_1-3, respectively) was centrifuged, and washed several times with ethanol solution. The loading amount of DOX was determined by the UV/Vis spectroscope at 480 nm. The loading efficiency (LE wt %) of DOX can be calculated by using the formula (1). The experiment repeated three times.

$$\text{LE wt\%}=\frac{m_{(\text{original DOX})}-m_{(\text{residual DOX})}}{m_{(Fe_3O_4@mSiO_2)}+m_{(\text{original DOX})}-m_{(\text{residual DOX})}+m_{(\text{R-S-S-R1})}}\times 100\% \quad (1)$$

Drug release

Gating protocol was investigated by studying the release profiles of DOX from the DOX-Fe_3O_4@mSiO_2@R-S-S-R_1 at pH 6.5 PBS buffer solution with 10 mM GSH or without GSH. Briefly, DOX-Fe_3O_4@mSiO_2@R-S-S-R_1 (30 mg) was dispersed in 5 mL of media solution and sealed in a dialysis bag (molecular weight cutoff 8000), which was submerged in 50 mL of media solution. At interval time, the solution was taken out to determine the release amount by UV.

Cell culture

HeLa cells (cervical cancer cell line) and Human umbilical vein endothelial cells(HUVEC) were grown in monolayer in Dulbecco's Modified Eagle's Medium (DMEM, Gibco) supplemented with 10 % (v/v) fetal bovine serum (FBS, Tianhang bioreagent Co., Zhejiang) and penicillin/streptomycin (100 U mL^{-1} and 100 μg mL^{-1}, respectively, Gibco) in a humidified 5 % CO_2 atmosphere at 37 ℃.

Confocal laser scanning microscopy (CLSM)

To check cellular uptake, HeLa cells were cultured in a 12-well chamber slide with one piece of cover glass at the bottom of each chamber in the incubation medium (DMEM) for 24 h. The cell nucleus was labeled by Hoechst 33342. DOX-Fe_3O_4@mSiO_2@R-S-S-R_1-2 was added into the incubation medium at the concentration of 100 μg mL^{-1} for 6 h incubation in 5 % CO_2 at 37 °C. After the medium was removed, the cells were washed twice with PBS (pH 7.4) and the cover glass was visualized under a laser scanning confocal microscope (FluoView FV1000, Olympus).

Cell viability

The viability of cells in the presence of nanoparticles was investigated using 3-[4,5-dimethylthialzol-2-yl]-2,5-diphenyltetrazolium bromide (MTT, Sigma) assay. The assay was performed out in triplicate in the following manner. For MTT assay, HeLa cells and HUVEC were seeded into 96-well plates at a density of 1×10^4 per well in 100 μL of media and grown overnight. The cells were then incubated with various concentration of Fe_3O_4@mSiO_2, Fe_3O_4@mSiO_2@R-S-S-R_1-2 and

DOX-Fe_3O_4@mSiO_2@R-S-S-R_1-2 for 24 h. Afterwards, cells were incubated in media containing 0.5 mg mL^{-1} of MTT for 4 h. The precipitated formazan violet crystals were dissolved in 100 μL of 10 % SDS in 10 mmol HCl solution at 37 ℃ overnight. The absorbance was measured at 570 nm by multi-detection microplate reader (SynergyTM HT, BioTek Instruments Inc, USA).

Characterization

Powder X-ray patterns (XRD) were recorded on a SIEMENSD 5005 X-ray diffractometer with Cu Kα radiation (40 kV, 30 mA). The nitrogen adsorption/desorption, surface areas, and median pore diameters were measured using a Micromeritics ASAP 2010M sorptometer. Surface area was calculated according to the conventional BET method and the adsorption branches of the isotherms were used for the calculation of the pore parameters using the BJH method. Fourier transform infrared (FTIR) spectra were recorded on a Perkin-Elmer 580B Infrared Spectrophotometer using the KBr pellet technique. A UV-vis spectrum was used to describe the amount of the drug release (SHIMADZU UV2550 spectrophotometer). Transmission electron microscopy (TEM) images were recorded on TECNAI F20. Zeta potential and dynamic light scattering (DLS) was carried out with ZetaPALS Zeta Potential Annlyzer. The magnetic properties of samples were characterized with a Vibrating Sample Magnetometer (Lake Shore 7410).

Results and discussion

Morphology and structure

X-ray diffraction patterns of Fe_3O_4@mSiO_2, DOX-Fe_3O_4@mSiO_2@R-S-S-R_1-1,

DOX-Fe_3O_4@mSiO_2@R-S-S-R_1-2, and DOX-Fe_3O_4@mSiO_2@R-S-S-R_1-3 powders are presented in Fig. 1. As can be seen in Fig. 1, all the samples reveal only one diffraction peak at about 2 θ= 2.26, suggesting they possesses the mesoporous structure. Moreover, after drug loading and R-S-S-R_1 grafting, the diffraction intensities of DOX-Fe_3O_4@mSiO_2@R-S-S-R_1s decrease obviously. Besides, the more amounts R-S-S-R_1 is grafted onto the Fe_3O_4@mSiO_2, the lower diffraction intensity the DOX-Fe_3O_4@mSiO_2@R-S-S-R_1s have, which is consistent with the previous report.[42]

The morphologies, particle sizes, and pores were investigated through TEM analysis. As displayed in Fig. 2A, Fe_3O_4 nanoparticles show the dispersed and uniform spherical morphology with the average diameter about 20 nm in size. Fe_3O_4@mSiO_2 reveals the obvious Fe_3O_4 core encapsulated by 20 nm silica shell with worm-like porous structure (Fig. 2B) which agrees with the corresponding XRD analysis (Fig. 1). As illustrated in Fig. 2C, the graft of organic "gate" results in the rough surface and less dispersion of these nanoparticles.

The pore structure and related textural properties of Fe_3O_4@mSiO_2 and DOX-Fe_3O_4@mSiO_2@R-S-S-R_1s were investigated through nitrogen adsorption-desorption measurements. The corresponding adsorption isotherms and the pore size distribution curves are depicted in Fig. 3. From Fig. 3A, Fe_3O_4@mSiO_2 displays the typical IV adsorption isotherm and a steep capillary condensation step at a relative pressure of P/P_0= 0.2-0.4. The typical H4 hysteresis loop is observed, testifying the mesoporous structure of Fe_3O_4@mSiO_2. As can be seen in Fig. 3A,

there is much smaller uptakes amount for DOX-Fe_3O_4@$mSiO_2$@R-S-S-R_1s if taking its counterpart (Fe_3O_4@$mSiO_2$) as a comparison. That also makes the surface area and pore volume decrease from 326 m^2 g^{-1} and 0.285 cm^3 g^{-1} of Fe_3O_4@$mSiO_2$ to 115 m^2 g^{-1} and 0.118 cm^3 g^{-1} of DOX-Fe_3O_4@$mSiO_2$@R-S-S-R_1-1, 63.1 m^2 g^{-1} and 0.0839 cm^3 g^{-1} of DOX-Fe_3O_4@$mSiO_2$@R-S-S-R_1-2, 43.4 m^2 g^{-1} and 0.0605 cm^3 g^{-1} of DOX-Fe_3O_4@$mSiO_2$@R-S-S-R_1-3, respectively (Table 1). Furthermore, as displayed in Table 1, it is worth mentioned that with the highest packages of R-S-S-R_1, DOX-Fe_3O_4@$mSiO_2$@R-S-S-R_1-3 possesses the lowest surface area and pore volume.

The FTIR absorption spectrum measurement was carried out to investigate the presence of R-S-S-R_1 grafting after the modification. The corresponding FT-IR spectra of R-S-S-R, R-S-S-R-APTES, Fe_3O_4@$mSiO_2$ and Fe_3O_4@$mSiO_2$@R-S-S-R_1 are illustrated in Fig. 4. As depicted in Fig. 4A, the absorption bands at 1689 and 1662 cm^{-1} are assigned to the C=O stretching vibration of dicarboxylic acids, and the O-H deformation vibration and C-O stretching vibration bands at 1440 and 1290 cm^{-1} also can be found, obviously. Furthermore, the absorption bands at 1200 and 1599 cm^{-1} are assigned to the C-O stretching vibration and C=C stretching vibration of phenol, respectively. Moreover, the absorption band of S-S at 535 cm^{-1} appears in R-S-S-R, testifying that R-S-S-R has been successfully synthesized. After the link of APTES, two new peaks at 1078 (Si-O stretching vibration) and 1579 cm^{-1} (N-H formation vibration) appear, confirming that R-S-S-R-APTES has been successfully synthesized. As shown in Fig. 4B, comparing Fe_3O_4@$mSiO_2$@R-S-S-R_1 with Fe_3O_4@$mSiO_2$, the

obvious absorption bands at 1661 cm^{-1}, which is assigned to the C=O stretching vibration of acid amide, can verify the successful grafting of R-S-S-R_1 on Fe_3O_4@$mSiO_2$.

Besides, the hydrodynamic diameters of Fe_3O_4@$mSiO_2$ and Fe_3O_4@$mSiO_2$@R-S-S-R_1-2 were measured by Zeta Potential Analyzer. As displayed in Table 2, the hydrodynamic diameter of Fe_3O_4@$mSiO_2$ centers at 82 nm that is larger than that observed from TEM because of the hydrate layer in aqueous environment. And that increases to 107.4 nm after the functional graft with R-S-S-R_1 shell. In addition, the corresponding zeta-potential was further used to monitor the surface change between Fe_3O_4@$mSiO_2$ and Fe_3O_4@$mSiO_2$@R-S-S-R_1s. From Fig. 5, Fe_3O_4@$mSiO_2$ shows the zeta-potential of -15.01 ± 1.17 mV derived from the negative charge of surface Si-OH, while that increases to 5.22 ± 1.91, 8.94 ± 0.91 mV, and 10.45 ± 1.26 of Fe_3O_4@$mSiO_2$@R-S-S-R_1-1, Fe_3O_4@$mSiO_2$@R-S-S-R_1-2, and Fe_3O_4@$mSiO_2$@R-S-S-R_1-3, respectively, due to the decrease of surface Si-OH substituted by R-S-S-R_1. Based on the above investigation, it is testified that R-S-S-R_1 has been successfully grafted on the surface of Fe_3O_4@$mSiO_2$.

Fig. 6 presents the magnetization characterization of Fe_3O_4@$mSiO_2$@R-S-S-R_1-1, Fe_3O_4@$mSiO_2$@R-S-S-R_1-2, and Fe_3O_4@$mSiO_2$@R-S-S-R_1-3 at room temperature. The hysteresis loops (Fig. 6) indicate the super-paramagnetism of all materials. Furthermore, the saturation magnetizations (*M*s) of Fe_3O_4@$mSiO_2$@R-S-S-R_1-1, Fe_3O_4@$mSiO_2$@R-S-S-R_1-2, and Fe_3O_4@$mSiO_2$@R-S-S-R_1-3 about 20.9, 15.1, and 9.08 emu g^{-1}, respectively, that is ascribed to the non-magnetic $mSiO_2$ and R-S-S-R_1.

Drug loading and release profiles

To investigate the sensitive controlled release kinetics of DOX-Fe_3O_4@$mSiO_2$@R-S-S-R_1s systems, DOX was selected as the model drug to evaluate the loading and controlled release behaviors. The actual loading capacity of DOX is calculated to be 1.23 ± 0.4, 1.60 ± 0.3 and 2.16 ± 0.5 wt % for DOX-Fe_3O_4@$mSiO_2$@R-S-S-R_1-1, DOX-Fe_3O_4@$mSiO_2$@R-S-S-R_1-2 and DOX-Fe_3O_4@$mSiO_2$@R-S-S-R_1-3, respectively. The *in vitro* release profile of DOX from DOX-Fe_3O_4@$mSiO_2$@R-S-S-R_1 in PBS buffer (pH 6.5) in response to GSH (10 mM in PBS) is shown in Fig. 7A. As can be seen in Fig. 7A, without GSH, DOX-Fe_3O_4@$mSiO_2$@R-S-S-R_1 nanoparticles release little cargo, below 25 % at 24 h. However, DOX can be released freely with the aid of GSH. As displayed in Fig. 7A, it takes 4 h to reach 45.16 %, 36.50 %, and 10.90 % and about 24 h to reach the maximal amount 94.89 %, 69.06 %, and 42.76 % for DOX-Fe_3O_4@$mSiO_2$@R-S-S-R_1-1, DOX-Fe_3O_4@$mSiO_2$@R-S-S-R_1-2 and DOX-Fe_3O_4@$mSiO_2$@R-S-S-R_1-3, respectively. The selective release is ascribed to the activity of the "gate". It is known that, -S-S- is a typical sensitive bond to some reduce agents, such as GSH, which can induce the bond breaking and "gate" open and drug release. Without GSH, R-S-S-R_1 blocks the pores of $mSiO_2$ encapsulate the cargo within the pores. Furthermore, the release performance of DOX-Fe_3O_4@$mSiO_2$ (without "gate") in pH 6.5 with and without GSH was also studied. As illustrated in Fig. 7A, the release of DOX from DOX-Fe_3O_4@$mSiO_2$ is faster than that from DOX-Fe_3O_4@$mSiO_2$@R-S-S-R_1. Moreover, there is not obvious difference between

the DOX release from DOX-Fe_3O_4@$mSiO_2$ with GSH or not. Based on the above investigation, the controlled drug release lies on the "-S-S- gate" sensitive to GSH. Without GSH or "-S-S- gate", the controlled drug release performance can be obtained. And the sensitive releases were further studied by the analysis of the hydrodynamic diameters and zeta-potentials before and after Fe_3O_4@$mSiO_2$@R-S-S-R_1s were treated by GSH. From Table 2, the hydrodynamic diameter increases from 107.4 to 110.3 nm, ascribing to the breaking of -S-S- outside Fe_3O_4@$mSiO_2$@R-S-S-R_1-2. Furthermore, the zeta-potential also reduced from 5.22 ± 1.91, 8.94 ± 0.91, and 10.45 ± 1.26 mV to -2.64 ± 1.78, -0.97 ± 1.14, and 1.25 ± 1.84 mV, respectively due to the breaking of -S-S- to form -SH (Fig. 5).

To further investigate the release behavior, the release data are analyzed by Higuchi model.[43,44] As we known, drug release kinetics from an insoluble, porous carrier matrix are frequently described by the Higuchi model, and the release rate can be described by the follow Equation:

$$Q = k * t^{1/2}$$

Where Q is the quantity of drug released from the materials, *t* denotes time, and *k* is the Higuchi dissolution constant. According to the model, for a purely diffusion-controlled process, the linear relationship is valid for the release of relatively small molecules distributed uniformly throughout the carrier.[44]

As illustrated in Fig. 7B, DOX-Fe_3O_4@$mSiO_2$@R-S-S-R_1-1 and DOX-Fe_3O_4@$mSiO_2$@R-S-S-R_1-2 exhibit a two-step release (0-8 h and 8-24 h) based upon the Higuchi model. While DOX-Fe_3O_4@$mSiO_2$@R-S-S-R_1-3 displays a

one-step release until 24 h. In the first 8 h, DOX-Fe_3O_4@$mSiO_2$@R-S-S-R_1-1 possess the highest dissolution constant *k* (the slope of the fitting line), followed with DOX-Fe_3O_4@$mSiO_2$@R-S-S-R_1-2 and DOX-Fe_3O_4@$mSiO_2$@R-S-S-R_1-3. That is because when DOX-Fe_3O_4@$mSiO_2$@R-S-S-R_1s was immersing in the release media with GSH, which induce -S-S- break and drug release. With the lowest amount of R-S-S-R_1, the "gatekeeper" was degraded most quickly, making the highest dissolution constant *k* as well as the fastest release rate of DOX-Fe_3O_4@$mSiO_2$@R-S-S-R_1-1. And in the second release step (8-24 h), the release rates of DOX-Fe_3O_4@$mSiO_2$@R-S-S-R_1-1 and DOX-Fe_3O_4@$mSiO_2$@R-S-S-R_1-2 decrease, and tend to similar to each other. It is believed that in the first release step most drug molecules release out side after "gatekeeper" was broken. That is to say the first release step depends mainly upon the degradation of -S-S- and the second release step determined just by the mesoporous structure of the host. However, with highest amount of R-S-S-R_1, the break of the "gatekeeper" become slowly, which is associated with the mesoporous structure to control the resistant release, so that DOX-Fe_3O_4@$mSiO_2$@R-S-S-R_1-3 displays a first-step release behavior until 24 h. To sum up, the amount of "gate" (R-S-S-R_1) can be used to regulate the release performance of the system.

***In vitro* cytotoxic effect and cellular uptake**

To investigate the cellular uptake of the sample, DOX-Fe_3O_4@$mSiO_2$@R-S-S-R_1-2 was incubated with HeLa cells at the concentration of 100 μg mL^{-1} for 6 h. The cellular uptake and subsequent localization of the sample is shown in Fig. 8. As

depicted in Fig. 8, nanoparticles are localized in the cytoplasm after 6 h incubated with HeLa cells, proving the fast cellular uptake ability of the sample, ascribing to the small particle size (65 nm) which is benefit to enter into the cell and enhance the drug efficacy.[45,46] In addition, DOX can be also found in cytoplasm after 6 h incubated that benefit from the fast cellular uptake ability of these nanocomposites and the low-pH endosomal environment.[47] Importantly, the morphology of HeLa cells was not influenced by the addition of DOX-Fe_3O_4@$mSiO_2$@R-S-S-R_1-2, also illustrating the well biocompatibility of the nanocomposites.

The investigation of the cytotoxicity of the synthesized drug carrier is significant for its potential biomedical applications. Only nontoxic carriers are suitable for drug delivery. Here the cellular toxicity of Fe_3O_4@$mSiO_2$, Fe_3O_4@$mSiO_2$@R-S-S-R_1-2, and DOX-Fe_3O_4@$mSiO_2$@R-S-S-R_1-2 nanoparticles toward HeLa cells were determined by means of a standard MTT cell assay. It could be seen that both pure Fe_3O_4@$mSiO_2$ and Fe_3O_4@$mSiO_2$@R-S-S-R_1-2 show no significant cytotoxic effect on the HeLa cells in a range of concentration (3.125-50 μg mL^{-1}). As can be seen in Fig. 9, the cell viability attains 86.14 % even the concentration of the Fe_3O_4@$mSiO_2$@R-S-S-R_1-2 reaches 50 μg mL^{-1}, while that of DOX-Fe_3O_4@$mSiO_2$@R-S-S-R_1-2 dereases to 58.79 % death (50 μg mL^{-1}). This can be explained by the fact that the nanoparticles can diffuse into cells rapidly, followed by the enzyme (GSH) inducing-release of the anticancer drug DOX to make the higher cytotoxicity of DOX-Fe_3O_4@$mSiO_2$@R-S-S-R_1-2. In order to validate the specificity of the enzyme dependent drug release, DOX-Fe_3O_4@$mSiO_2$@R-S-S-R_1-2

incubated with a non-cancerous cell line (HUVEC) is presented as the control. As illustrated in Fig. 9, it shows very low cytotoxic effect (about 28.40 %) on the HUVEC even when the concentration of the cells attains to 50 μg mL^{-1}due to the lack of GSH to enhance DOX release.

Conclusion

In summary, we have demonstrated an enzyme-responsive controlled-release system using a smart switch (R-S-S-R_1) gated core-shell Fe_3O_4@$mSiO_2$ nanomaterials for targeted drug delivery. Owing to the degradation of "gate", the cargos can release triggered by GSH, a specific enzyme which has been proved to be highly expressed at the tumor microenvironment. The *in vitro* efficacy of the nanocomposites were confirmed using HeLa cells and the MTT and CLSM were carried out, revealing that the nanocarrier can fast enter into cells and no obvious cytotoxic effect on HeLa cells at a concentration of 50 μg mL^{-1}. Furthermore, the drug molecules can be transported in to cells just after 6 h incubation with HeLa. With considering the high specificity and good controlled-release performance, DOX-Fe_3O_4@$mSiO_2$@R-S-S-R_1 can be employed as a potential candidature for targeted cancer treatment.

Acknowledgments

Financial support for this study was provided by the National Natural Science Foundation of China (21471041, 21171045, 21101046, 21441002), Natural Science Foundation of Heilongjiang Province of China ZD201214，Technology development pre-project of Harbin Normal University (12XYG-11).

References

1 F. S. Du, Y. Wang, R. Zhang and Z. C. Li, *Soft Matter,* 2010, **6**, 835-848.

2 J. Wu, Y. J. Zhu, F. Chen, X. Y. Zhao, J. Zhao and C. Qi, *Dalton. Trans.*, 2013, **42**, 7032-7040.

3 X. Q. An, F. Zhan and Y. Y. Zhu, *Langmuir*, 2013, **29**, 1061-1068.

4 T. Levis and V. Ganesan, *Soft Matter*, 2012, **8**, 11817-11830.

5 A. Shimoda, S. I. Sawada, A. Kano, A. Maruyama, A. Moquin, F. M. Winnik and K. Akiyoshi, *Colloid. Surface. B.*, 2012, **99**, 38-44.

6 H. Kim, S. Kim, C. Park, H. Lee, H. J. Park and C. Kim, *Adv. Mater.*, 2010, **22**, 4280-4283.

7 Y. N. Zhao, B. G. Trewyn, I. I. Slowing and V. S-Y. Lin, *J. Am. Chem. Soc.*, 2009, **131**, 8398-8400.

8 B. G. Trewyn, I. I. Slowing, S. Giri, H. T. Chen and V. S. Y. Lin, *Acc. Chem. Res.*, 2007, **40**, 846-853.

9 J. Lu, M. Liong, Z. X. Li, J. I. Zink and F. Tamanoi, *Small*, 2010, **6**, 1794-1805.

10 H. Yamada, C. Urata, Y. Aoyama, S. Osada, Y. Yamauchi and Kuroda, K. *Chem. Mater.*, 2012, **24**, 1462-1471.

11 L. Yuan, Q. Tang, D. Yang, J. Z. Zhang, F. Zhang and J. Hu, *J. Phys. Chem. C.*, 2011, **115**, 9926-9932.

12 X. F. Guo, Y. S. Kim and G. J. Kim, *J. Phys. Chem. C.*, 2009, **113**, 8313-8319.

13 M. Manzano and M. Vallet-Regi, *J. Mater. Chem.*, 2010, **20**, 5593-5604.

14 Y. J. Wang and F. Caruso, *Chem. Mater.*, 2005, **17**, 953-961.

15 B. S. Chang, D. Chen, Y. Wang, Y. Z. Chen, Y. F. Jiao, X. Y. Sha and W. L. Yang, *Chem. Mater.*, 2013, **25**, 574-585.

16 M. W. Ambrogio, C. R. Thomas, Y-L. Zhao, J. I. Zink and J. F. Stoddart, *Acc. Chem. Res.*, 2011, **44**, 903-913.

17 S. Angelos, N. M. Khashab and Y-W Yang, *J. Am. Chem. Soc.*, 2009, **131**, 12912-12914.

18 B. S. Chang, X. Y. Sha, J. Guo, Y. F. Jiao, C. C. Wang and W. L. Yang, *J. Mater. Chem.*, 2011, **21**, 9239-9247.

19 E. Aznar, M. D. Marcos, R. Martinez-Manez, F. Sancenon, J. Soto, P. Amoros and C. Guillem, *J. Am. Chem. Soc.*, 2009, **131**, 6833-6843.

20 Y. Zhu, W. Meng, H. Gao and N. Hanagata, *J. Phys. Chem. C.*, 2011, **115**, 13630-13636.

21 H. Li, L. L. Tan, P. Jia, Q. L. Li, Y. L. Sun, J. Zhang, Y. Q. Ning, J. H. Yu and Y. W. Yang, *Chem. Sci.*, 2014, **5**, 2804-2808.

22 F. Muhammad, M. Y. Guo, W. X. Qi, F. X. Sun, A. F. Wang, Y. J. Guo and G. S. Zhu, *J. Am. Chem. Soc.*, 2011, **133**, 8778-8781.

23 I. Ojima, *Acc. Chem. Res.*, 2008, **41**, 108-119.

24 I. Ojima, X. D. Geng, X. Y. Wu, C. X. Qu, C. P. Borella, H. S. Xie, S. D. Wilhelm, B. A. Leece, L. M. Bartle, V. S. Goldmacher and R. V. J. Chari, *J. Med. Chem.*, 2002, **45**, 5620-5623.

25 N. S. Kosower and E. M. Kosower, *Int. Rev. Cytol.*, 1978, **54**, 109-160.

26 S. J. Yu, C. L. He, J. X. Ding, Y. L. Cheng, W. T. Song, X. L. Zhuang and X. S.

Chen, *Soft Matter*, 2013, **9**, 2637-2645.

27 J. A. Cook, H. I. Pass, S. N. Iype, N. Friedman, W. Degraff, A. Russo and J. B. Mitchell, *Cancer. Res.*, 1991, **51**, 4287-4294.

28 S. L. Blair, P. Heerdt, S. Sacher, A. Abolhoda, S. Hochwald, H. Cheng and M. Burt, *Cancer. Res.*, 1997, **57**, 152-155.

29 R. Weissleder, A. Bogdanov, E. A. Neuwelt and M. Papisov, *Adv. Drug Del. Rev.*, 1995, **16**, 321-334.

30 J. Su, M. Cao, L. Ren and C. Hu, *J. Phys. Chem. C.*, 2011, **115**, 14469-14477.

31 X. Li, X. Huang, D. Liu, X. Wang, S. Song, L. Zhou and H. Zhang, *J. Phys. Chem. C.*, 2011, **115**, 21567-21573.

32 E. Taboada, E. Rodríguez, A. Roig, J. Oró, A. Roch and R. N. Muller, *Langmuir*, 2007, **23**, 4583-4588.

33 E. Ruiz-Hernández, A. López-Noriega, D. Arcos, I. Izquierdo-Barba, O. Terasaki, and M. Vallet-Regí, *Chem. Mater.*, 2007, **19**, 3455-3463.

34 J. Zhou, W. Wu, D. Caruntu, M. H. Yu, A. Martin, J. F. Chen, C. J. O'Connor and W. L. Zhou, *J. Phys. Chem. C.*, 2007, **111**, 17473-17477.

35 Y. Zhu, T. Ikoma, N. Hanagata and S. Kaskel, *Small*, 2010, **6**, 471-478.

36 M. Liong, J. Lu, M. Kovochich, T. Xia, S. G. Ruehm, A. E. Nel, F. Tamanoi and J. I. Zink, *ACS Nano*, 2008, **2**, 889-896.

37 P. P. Yang, S. L. Gai and J. Lin, *Chem. Soc. Rev.*, 2012, **41**, 3679-3698.

38 Z. B. Zheng and D. J. Creighton, *Bioconjugate. Chem.*, 2005, **16**, 598-607.

39 J. Park, K. An, Y. H. Wang, J. G. Park, H. J. Noh, J. Y. Kim, T. Hyeon, *Nature*

materials, 2004, **3**, 891-895.

40 S. Saphier, A. Haft and S. Margel, *J. Med. Chem.*, 2012, **55**, 10781-10785.

41 D. A. Kennedy, N. Vembu, F. R. Fronczek and M. Devocelle, *J. Org. Chem.*, 2011, **76**, 9641-9647.

42 W. Guo, C. Y. Yang, L. R. Cui, H. M. Lin and F. Y. Qu, *Langmuir*, 2014, **30**, 243-249.

43 T. Higuchi, *J Pharm Sci.*, 1961, **50**, 874-875.

44 T. Higuchi, *J Pharm Sci.*, 1963, **52**, 1145-1149.

45 X. J. Song, H. Gong, S. N. Yin, L. Cheng, C. Wang, Z. W. Li, Y. G. Li, X. Y. Wang, G. Liu and Z. Liu, *Adv. Funct. Mater.*, 2014, **24**, 1194-1201.

46 L. M. Pan, Q. J. He, J. N. Liu, Y. Chen, M. Ma, L. L. Zhang and J. L. Shi, *J. Am. Chem. Soc.*, 2012, **134**, 5722-5725.

47 X. Zhang, P. P. Yang, Y. L. Dai, P. A. Ma, X. J. Li, Z. Y. Cheng, Z. Y. Hou, X. J. Kang, C. X. Li and J. Lin, *Adv. Funct. Mater.*, 2013, **23**, 4067-4078.

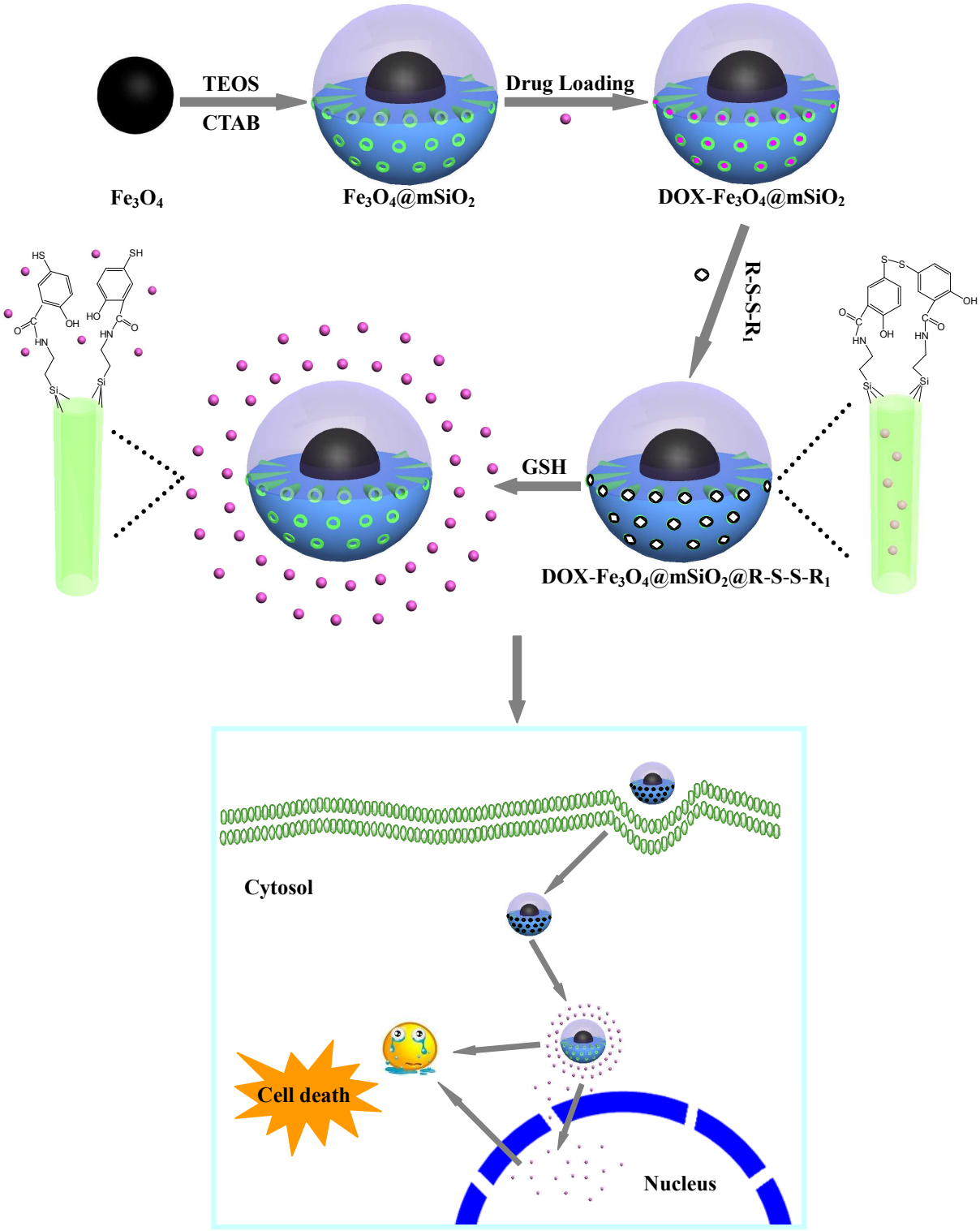

Scheme 1

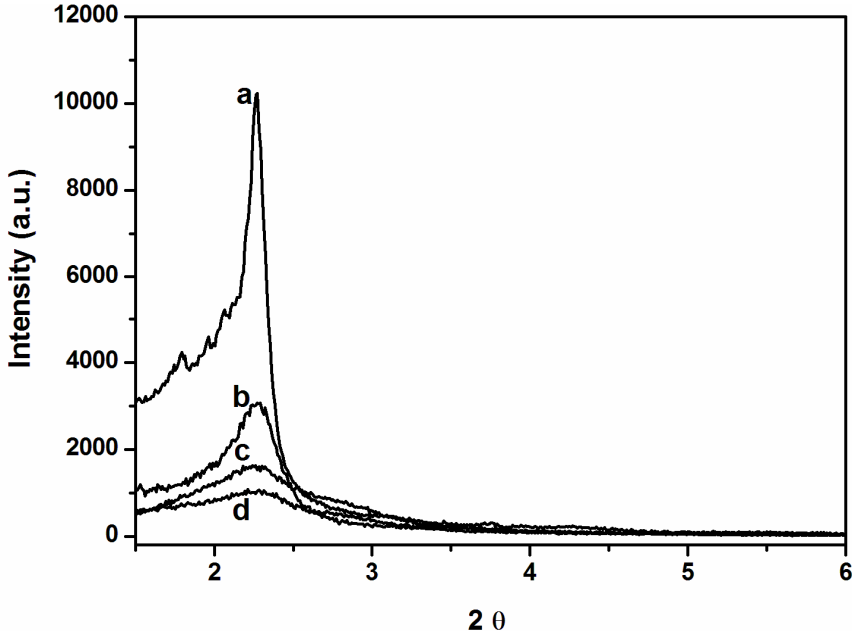

Fig. 1

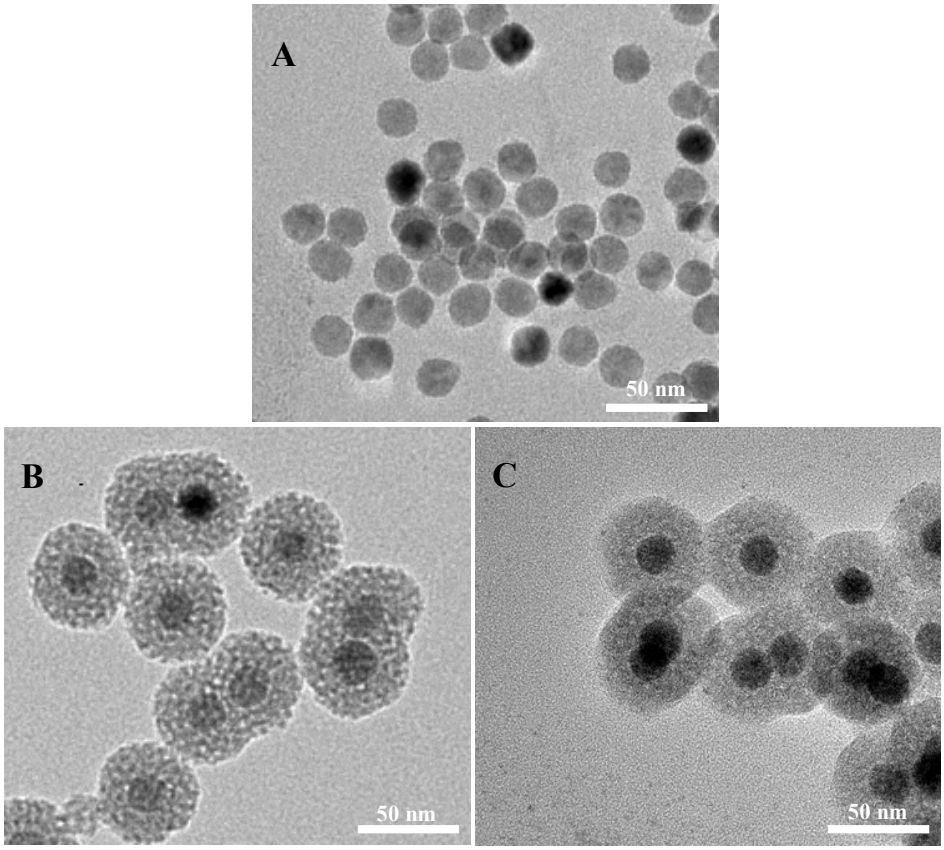

Fig. 2

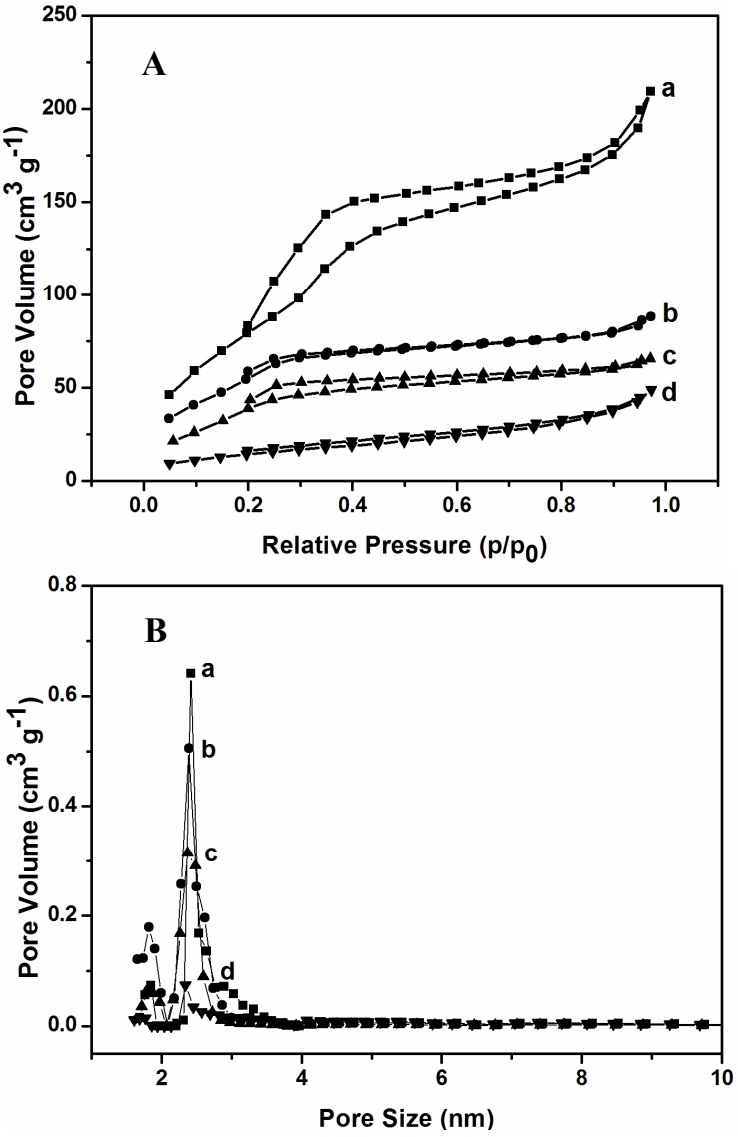

Fig. 3

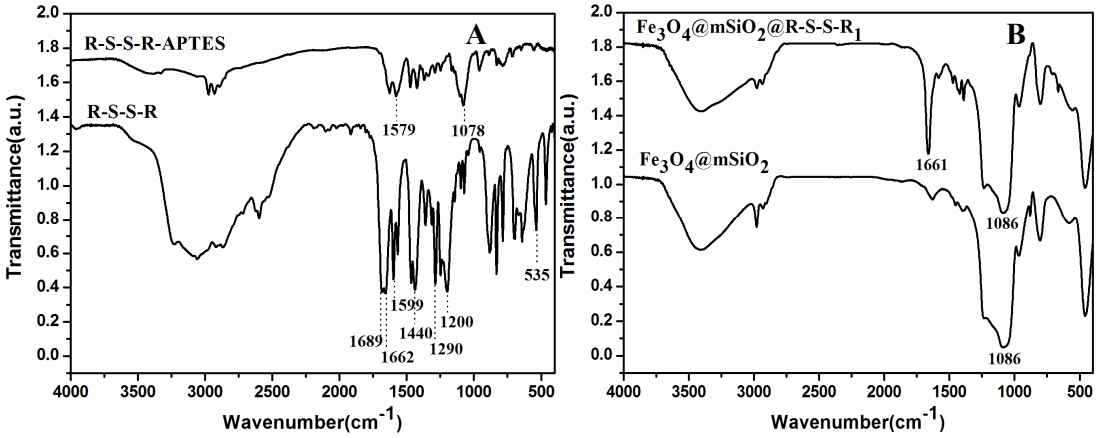

Fig. 4

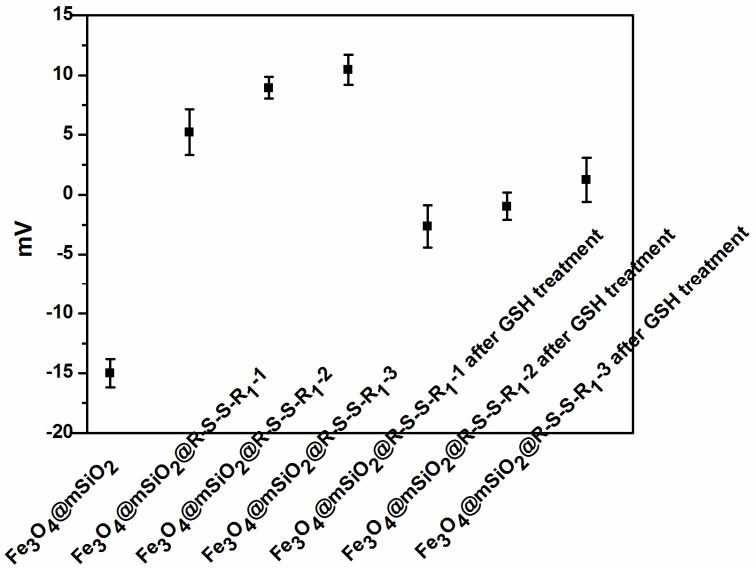

Fig. 5

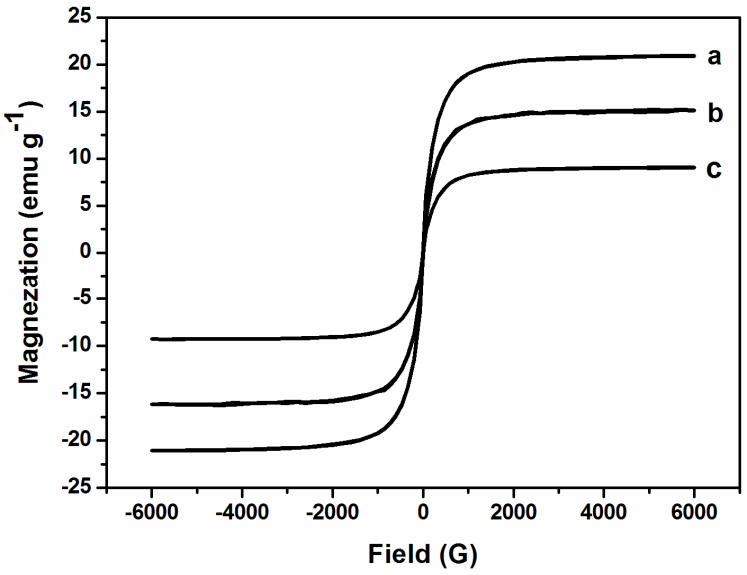

Fig. 6

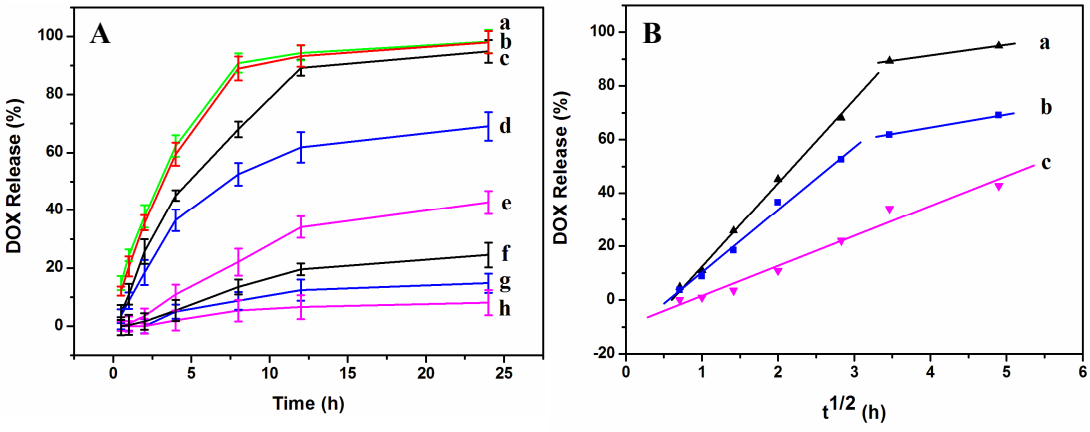

Fig. 7

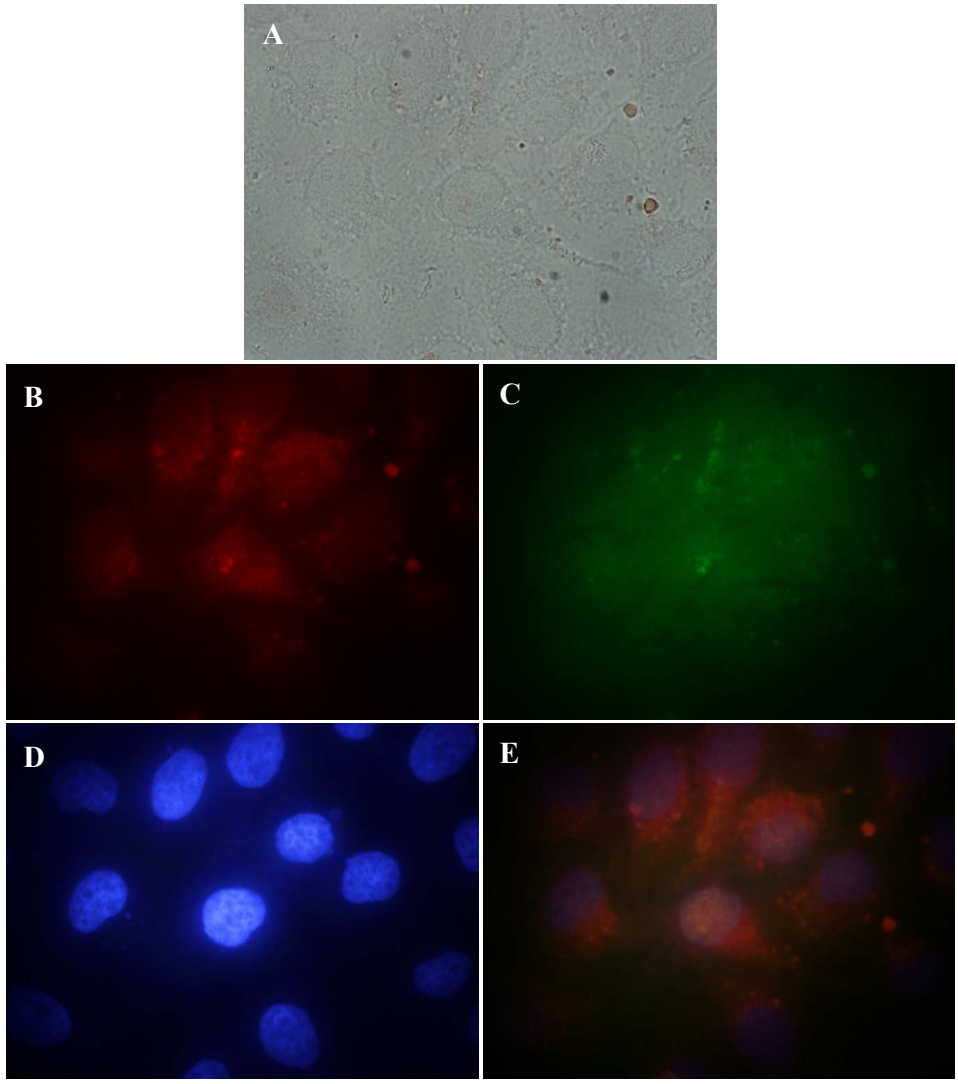

Fig. 8

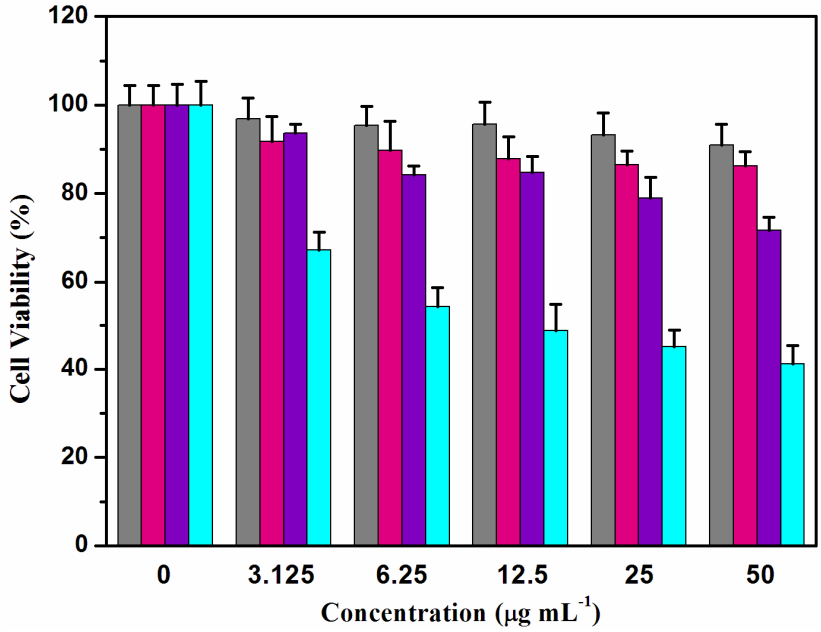

Fig. 9

Table 1 Pore parameters and loading efficiency of the samples

Samples	BET ($m^2 g^{-1}$)	V_p ($cm^3 g^{-1}$)	Pore Size (nm)
Fe_3O_4@$mSiO_2$	326	0.285	2.42
DOX-Fe_3O_4@$mSiO_2$@R-S-S-R_1-1	115	0.118	2.39
DOX-Fe_3O_4@$mSiO_2$@R-S-S-R_1-2	63.1	0.0839	2.37
DOX-Fe_3O_4@$mSiO_2$@R-S-S-R_1-3	43.4	0.0605	2.33

Table 2 Hydrodynamic size of the samples

Samples	Hydrodynamic size distribution (nm)
Fe_3O_4@$mSiO_2$	82.0
Fe_3O_4@$mSiO_2$@R-S-S-R_1-2	107.4
Fe_3O_4@$mSiO_2$@R-S-S-R_1-2 after GSH treatment	110.3

Captions:

Scheme 1 Illustration of the preparation and controlled release process of DOX-Fe_3O_4@$mSiO_2$@R-S-S-R_1.

Fig. 1 Low-angle XRD patterns of (a) Fe_3O_4@$mSiO_2$, (b) DOX-Fe_3O_4@$mSiO_2$@R-S-S-R_1-1, (c) DOX-Fe_3O_4@$mSiO_2$@R-S-S-R_1-2, and (d) DOX-Fe_3O_4@$mSiO_2$@R-S-S-R_1-3.

Fig. 2 TEM images of A) Fe_3O_4, B) Fe_3O_4@$mSiO_2$, and C) Fe_3O_4@$mSiO_2$@R-S-S-R_1-2.

Fig. 3 (A) Nitrogen adsorption-desorption isotherms and (B) pore size distribution for (a) Fe_3O_4@$mSiO_2$, (b) DOX-Fe_3O_4@$mSiO_2$@R-S-S-R_1-1, (c) DOX-Fe_3O_4@$mSiO_2$@R-S-S-R_1-2, and (d) DOX-Fe_3O_4@$mSiO_2$@R-S-S-R_1-3.

Fig. 4 FTIR spectra of (A) R-S-S-R and R-S-S-R-APTES and (B) Fe_3O_4@$mSiO_2$ and Fe_3O_4@$mSiO_2$@R-S-S-R_1.

Fig. 5 Zeta-potential test of Fe_3O_4@$mSiO_2$, Fe_3O_4@$mSiO_2$@R-S-S-R_1-1, Fe_3O_4@$mSiO_2$@R-S-S-R_1-2, Fe_3O_4@$mSiO_2$@R-S-S-R_1-3, Fe_3O_4@$mSiO_2$@R-S-S-R_1-1 after R-S-S-R_1 degraded in pH 6.5 with GSH, Fe_3O_4@$mSiO_2$@R-S-S-R_1-2 after R-S-S-R_1 degraded in pH 6.5 with GSH, Fe_3O_4@$mSiO_2$@R-S-S-R_1-3 after R-S-S-R_1 degraded in pH 6.5 with GSH.

Fig. 6 Representative hysteresis-loop measurements of the obtained (a) Fe_3O_4@$mSiO_2$@R-S-S-R_1-1, (b) Fe_3O_4@$mSiO_2$@R-S-S-R_1-2, and (c) Fe_3O_4@$mSiO_2$@R-S-S-R_1-3.

Fig. 7 Release profiles of DOX from A) DOX-Fe_3O_4@$mSiO_2$ in pH 6.5 (a) with GSH, (b) without GSH, and DOX-Fe_3O_4@$mSiO_2$@R-S-S-R_1 in pH 6.5 with GSH (c) DOX-Fe_3O_4@$mSiO_2$@R-S-S-R_1-1, (d) DOX-Fe_3O_4@$mSiO_2$@R-S-S-R_1-2 (e) DOX-Fe_3O_4@$mSiO_2$@R-S-S-R_1-3, and DOX-Fe_3O_4@$mSiO_2$@R-S-S-R_1 in pH 6.5 without GSH, (f) DOX-Fe_3O_4@$mSiO_2$@R-S-S-R_1-1, (g) DOX-Fe_3O_4@$mSiO_2$@R-S-S-R_1-2, and (h) DOX-Fe_3O_4@$mSiO_2$@R-S-S-R_1-3; B) Higuchi plot for the release of DOX from DOX-Fe_3O_4@$mSiO_2$@R-S-S-R_1 in pH 6.5 with GSH, (a) DOX-Fe_3O_4@$mSiO_2$@R-S-S-R_1-1, (b) DOX-Fe_3O_4@$mSiO_2$@R-S-S-R_1-2, and (c) DOX-Fe_3O_4@$mSiO_2$@R-S-S-R_1-3.

Fig. 8 CLSM images of HeLa cells after incubation with 100 μg mL^{-1} DOX-Fe_3O_4@$mSiO_2$@R-S-S-R_1-2 for 6 h. (A) HeLa cells (bright), (B) DOX fluorescence in cells (red), (C) FITC labeled DOX-Fe_3O_4@$mSiO_2$@R-S-S-R_1-2 (green), (D) Hoechst 33342 labeled cell nucleus (blue), and (E) merged.

Fig. 9 Cell viability of HeLa cells incubated with different amounts of Fe_3O_4@$mSiO_2$ (gray), Fe_3O_4@$mSiO_2$@R-S-S-R_1-2 (pink), and DOX-Fe_3O_4@$mSiO_2$@R-S-S-R_1-2 (cyan), and Human umbilical vein endothelial cells (HUVEC) incubated with different amounts of DOX-Fe_3O_4@$mSiO_2$@R-S-S-R_1-2 (violet) for 24 h.